



ELSEVIER

Contents lists available at ScienceDirect

Computational Materials Science

journal homepage: www.elsevier.com/locate/commatsci

Plastic deformation of a porous bcc metal containing nanometer sized voids

C.J. Ruestes ^{a,e,f,*}, E.M. Bringa ^{a,b}, A. Stukowski ^c, J.F. Rodríguez Nieva ^d, Y. Tang ^f, M.A. Meyers ^f^a Instituto de Ciencias Básicas, Univ. Nac. de Cuyo, Mendoza 5500, Argentina^b CONICET, Mendoza 5500, Argentina^c Darmstadt University of Technology, Darmstadt, Germany^d Massachusetts Institute of Technology, MA 02139, USA^e Instituto Balseiro, Univ. Nac. de Cuyo, Bariloche 8400, Argentina^f University of California, San Diego, La Jolla, CA 92093, USA

ARTICLE INFO

Article history:

Received 29 October 2013

Received in revised form 31 January 2014

Accepted 28 February 2014

Available online 29 March 2014

Keywords:

Molecular dynamics

Dislocations

Nanoporous

Nanovoid

ABSTRACT

Nanoporous materials, can present an outstanding range of mechanical properties. Both molecular dynamics and dislocation analysis were used to evaluate and quantify the evolution of plasticity in a porous Ta single crystal containing randomly placed voids with 3.3 nm radii and average initial porosity of 4.1%, when subjected to uniaxial compressive strain. Nanovoids act as effective sources for dislocation emission. Dislocation shear loops nucleate at the surface of the voids and expand by the advance of the edge component. The evolution of dislocation configuration and densities were predicted by the molecular dynamics calculations and successfully compared to an analysis based on Ashby's concept of geometrically-necessary dislocations. Resolved shear stress calculations were performed for all bcc slip systems and used to identify the operating Burgers vectors in the dislocation loops. The temperature excursion during plastic deformation was used to estimate the mobile dislocation density which is found to be less than 10% of the total dislocation density.

© 2014 Elsevier B.V. All rights reserved.

1. Introduction

Metallic foams exhibit an outstanding range of properties obtained through the tailoring of void configuration and size [1–4]. The reduction in size of the voids in metals leads to high strength levels that are enabled by nanoscale effects. Biener et al. [1] demonstrated that nanoporous gold can reach a flow stress of 4.5 GPa. This is akin to the results of nanopillar strength by Greer et al. [5] and Nix et al. [6]. Kim et al. [7] also showed strong size effects in nanopillars (both in compression and tension) for various bcc metals, including Ta. In addition to the high strength achieved in nanofoams, their effectiveness in radiation resistance has been proposed. This is due to the size of the ligaments which, if properly chosen, produces a “self-healing” foam [3]. The nanoscale foams inhibit the formation of the collision cascade by providing sinks for the radiation induced defects. In addition to high porosity metallic foams as the ones described above, there are samples with low porosity at the nanoscale, like radiation damaged samples [8],

or pre-spalled samples [9,10], where mechanical properties of samples are also of interest.

In the last few decades there has been a tremendous advance in the understanding of plasticity under extreme conditions such as the high pressures and strain rates achievable by shock compression. The extremely high strain rates obtained with laser compression (10^7 – 10^9 s $^{-1}$) and the ultrashort durations (1–10 ns) of the pressure pulse render this technique a unique tool to explore extreme regimes of plastic deformation, pressure, strain rate and temperature. Although plastic deformation is being studied intensively experimentally through the characterization of recovered specimens, direct simulations provide important insights into the dynamic processes of plastic deformation. Experiments that probe pressure-induced nanovoid collapse at the relevant nanoscopic length and ultrashort time scales are extremely difficult or impossible with current set-ups, while continuum models might not work at the nanoscale. Reisman et al. [8] measured VISAR profiles of a sample with a collection of radiation-induced voids, and were able to reasonably fit their data using a dislocation-based model with a size-dependent plastic threshold for the voids. Several authors [11–13] showed how molecular dynamics simulations can be coupled with laser-driven shock experiments to provide

* Corresponding author at: University of California, San Diego, La Jolla, CA 92093, USA. Tel.: +1 858 900 8425.

E-mail address: cjuestes@hotmail.com (C.J. Ruestes).

insight into the plastic deformation mechanisms in such extreme regimes.

Despite these advances, nano-scale plasticity under extreme conditions remains poorly understood for bulk materials, and even more so for materials including porosity, where there are relatively few studies. Nanoscale porosity appears in many different scenarios: radiation damage [8], laser ablation [14], incipient spall [9], metallic and non-metallic nanofoams [15], etc. The understanding of the role of porosity on mechanical behavior is important for the assessment and development of materials such as metallic foams [1], and materials for new fission and fusion reactors [3], with improved mechanical properties.

Although there are a number of studies focusing on single voids in fcc [16–20] and bcc metals [21–25], void assemblies and the more general problem of a porous metal have not yet been thoroughly investigated in simulations, except for relatively few studies [10,18,26,27].

We aim to develop a mechanistic understanding of the microstructural changes induced by high strain rate compression of a material with nanoscale porosity. For that purpose, and given the typical size limitations of molecular dynamics, we chose to conduct this study by adding a few nanovoids to a bulk bcc Ta sample reaching a relatively low porosity (~4%) [26]. We found that dislocation production leads to an anomalous Taylor type relationship between dislocation density and stress, and that porosity collapse was directly related to plastic activity. In this study we focus on a detailed analysis of dislocation activity including activated dislocation systems and dislocation velocity, and present models to account for the lower plastic threshold, as compared to the case of a single void, and for the resulting density of geometrically necessary dislocations (GNDs). We also analyze plastic heating during void collapse and several other aspects of the evolution of the sample under compression. Although we are focusing here on a material with a low void fraction, the size of the voids and the acquired ligaments can be compared to those found in novel yet-laboratory scale nanofoams and therefore get that the conclusions reached herein can be extrapolated to higher porosities, in the regime of importance for both mechanical performance and radiation resistance.

2. Computational modeling

The compression simulations were performed with LAMMPS [28] and bcc Ta was modeled with an extended Finnis–Sinclair potential [29]. Based on static equilibrium simulations, this potential predicts pressure–volume relations comparable to experimental data [29]. It gives generalized stacking-fault energies comparable with ab initio results [24], and it has been used in previous work on void collapse [24–26], as well as rapid compression of bcc metals [30,31]. Non-equilibrium shock simulations are a challenge for empirical potentials because solid–solid phase transitions [32,33] or soft-phonon modes [34] may appear artificially. No artificial behavior that may affect our simulations is known for pressures under 60 GPa, being 50 GPa the maximum pressure reached in our studies.

The simulation domain was initially set up as a cubic sample containing 100^3 unit cells. Ten spherical voids with radii of ~3.3 nm were created inside the sample, with an average distance (between void surfaces) of 10.5 nm, resulting in a 4.1% volume fraction of voids and 1.9 million remaining atoms. Periodic boundary conditions were imposed in all directions. The sample was equilibrated to zero pressure at an initial temperature of 300 K.

A uniaxial compressive strain rate of 10^9 s^{-1} was applied in the [001] direction for 200 ps, resulting in a total of 20% volume strain. Lateral strains were impeded. This strain state simulates early

stages of laser shock compression experiments [11,12,35–37]. A 1 fs time step was chosen and the simulation was run with a constant NVE integration consistent with the micro-canonical ensemble. In this manner, no temperature control was imposed and we were able to measure temperature effects produced by plastic activity.

Defect tracking was done by means of the Common Neighbor Analysis (CNA) [38], a structural filter known to be suitable for bcc metals. During the computational run, non-bcc atoms were filtered by the built-in CNA available in LAMMPS. An improved version [39] of the recently developed dislocation extraction algorithm technique (DXA) [40], was also used to identify line and surface defects. Visualization of dislocations and void surfaces was performed using VMD [41] and ParaView [42].

3. Results

The computational procedures for the global stress–strain response and resolved shear stresses are explained in Sections 3.1 and 3.2 respectively. The dislocation activity is discussed in Section 3.3 and dislocation densities were computed independently in Section 3.4 (CNA), Section 3.5 (DXA), Section 3.6 (Mobile dislocation density) and Section 3.7 (geometrically-necessary dislocations).

3.1. Global uniaxial stress–strain response

The stress in the loading direction, σ_{zz} , was monitored during the simulation and is plotted in Fig. 1, next to the calculations of Tang et al. [24] for a sample of the same dimensions containing a single void of 3.3 nm radius. The stresses at the point where plastic flow starts are marked by arrows. As one might expect, the stress is about 20% lower in the sample with ten voids than for a single void. Wu and Markenscoff [43] calculated the singular stress amplification between two holes of equal radius r , showed in Fig. 2. The simplest form of this calculation is given, for uniaxial loading and at a point midway between the two holes, where this amplification, σ_{max} , is highest:

$$\sigma_{max} \sim \left[\frac{1.94}{\left(\frac{d}{2r}\right)^{\frac{1}{2}}} \pm \frac{\sqrt{2}}{2\left(\frac{d}{2r}\right)^{\frac{1}{2}}} \right] \sigma_\infty \quad (1)$$

where σ_∞ is the stress at an infinite distance from the holes, r is the hole radius, and d is the distance between the edges of the holes. The minus sign corresponds to the hole centers aligned with the

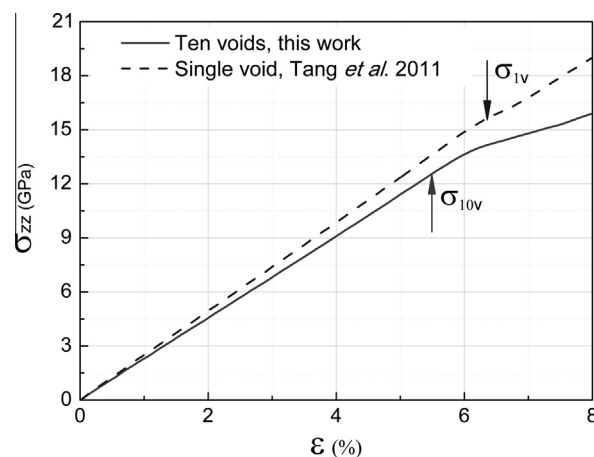


Fig. 1. Stress–strain curve for void collapse under uniaxial strain. Void radius is 3.3 nm. Yield strains at which defects start to nucleate are indicated by arrows. The elastic modulus reduction in our simulation is a direct consequence of the porosity.

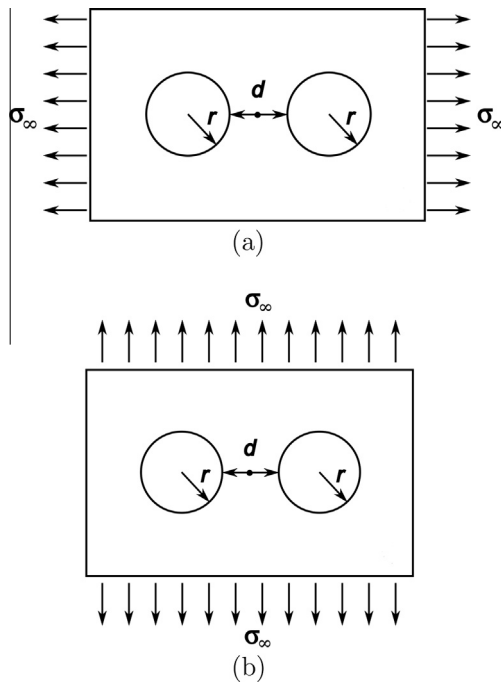


Fig. 2. Schematic showing interaction of two voids considered as limiting configurations by Wu and Markenscoff [43] (a) void center axis parallel to loading direction, and (b) normal to loading direction.

axis of loading and the plus sign to the perpendicular alignment. Fig. 2 shows the two configurations, considered as limits by Wu and Markenscoff [43]. Although this is a two-dimensional analysis, it provides a good first order estimate of the stress amplification. The case of multiple voids can be roughly approximated as the one for two voids, since the stress amplification decreases fairly rapidly with distance. In the present case, the average d is ~ 10.5 nm. Applying these values to Eq. (1), we obtain:

$$\sigma_{\max} \sim \sigma_\infty \quad (2)$$

for longitudinal tension (hole center axis parallel to loading) and

$$\sigma_{\max} \sim 2.1\sigma_\infty \quad (3)$$

for transverse tension (hole center axis normal to loading).

For a random arrangement of voids, we can assume that the amplification falls in between these two limiting cases. The measured ratio of the (remote) compressive stresses leading to dislocation nucleation for an isolated void, σ_{1v} [24] and the void assemblage, σ_{10v} , is consistent with the theoretical model described above:

$$\frac{\sigma_{1v}}{\sigma_{10v}} = \frac{15.5 \text{ GPa}}{13 \text{ GPa}} \sim 1.2 \quad (4)$$

Thus, the presence of voids leads to the creation of ligaments that amplify the local stresses and decrease the far field tractions required for dislocation loop emission. The closest void to the void where the first dislocation emission occurs is located roughly at 45° in a planar projection and, therefore, in between the limiting cases of longitudinal and transverse location, justifying our approximation of taking an average amplification stress.

3.2. Analysis of the resolved shear stresses

In the simulation setup, the sample was subjected to a uniaxial strain along [001] direction:

$$\epsilon_{ij} = \begin{bmatrix} 0 & 0 & 0 \\ 0 & 0 & 0 \\ 0 & 0 & \epsilon_{33} \end{bmatrix} \quad (5)$$

where ϵ_{33} is the elastic strain prior to the onset of plasticity. The corresponding stress state is obtained from,

$$\sigma_{ij} = C_{ijkl}\epsilon_{kl} \quad (6)$$

C_{ijkl} is the elastic stiffness matrix in the simulation coordinate system ([100],[010],[001]). For the Ta potential used [29], the stiffness matrix in GPa is:

$$C_{ijkl} = \begin{bmatrix} 230.8 & 143.5 & 143.5 & 0 & 0 & 0 \\ 143.5 & 230.8 & 143.5 & 0 & 0 & 0 \\ 143.5 & 143.5 & 230.8 & 0 & 0 & 0 \\ 0 & 0 & 0 & 91.3 & 0 & 0 \\ 0 & 0 & 0 & 0 & 91.3 & 0 \\ 0 & 0 & 0 & 0 & 0 & 91.3 \end{bmatrix} \quad (7)$$

Applying Eqs. (5) and (7) into Eq. (6), we obtain the principal stresses:

$$\sigma_{ij} = \begin{bmatrix} 143.5 & 0 & 0 \\ 0 & 143.5 & 0 \\ 0 & 0 & 230.8 \end{bmatrix} \epsilon_{33} (\text{GPa}) \quad (8)$$

The triaxial stress state requires an analysis more complete than the common Schmid factor computation. It is important to know the resolved shear stresses for the bcc slip systems since it is reasonable to expect that one or more of these systems will be activated once plasticity develops. Therefore, we proceed with a transformation as already applied by Cao and co-workers [44] to Cu crystals following the formulation available (e.g. [45]),

$$\sigma'_{ij} = l_{ik}l_{jl}\sigma_{kl} \quad (9)$$

where l_{ik} and l_{jl} are the cosines of the angles between the coordinate system of the slip plane and the crystallographic axes. Performing this transformation for the 48 bcc slip systems including the {110}, {112} and {123} families of slip planes allows us to calculate the resolved shear stresses in terms of ϵ_{33} . These values are reported in Table 1 for {110} and {112}, and Table 2 for {123}. The calculated values are an indication of the driving stress on the slip systems prior to plastic flow. The relative closeness of the resolved shear stress values for several slip systems in the three families gives further support to the peculiar character that was identified by Tang et al. [24]. The results presented in Tables 1 and 2 show that the four slip directions [111], [111], [111], and [111] (and their negatives [111], [111], [111], and [111]) are included in the systems with the highest resolved shear stresses. Considering, as an example, the [111] slip direction, the planes with highest resolved shear stress are:

Table 1

Resolved shear stresses on the 12 slip systems corresponding to families of {110} slip planes and 12 slip systems for families of {112} slip planes; uniaxial strain compression of tantalum along [001].

Slip plane {110}	RSS (GPa)	Slip plane {112}	RSS (GPa)
(011)[111]	$35.6 \epsilon_{33}$	(112)[111]	$41.1 \epsilon_{33}$
(011)[111]	$35.6 \epsilon_{33}$	(112)[111]	$41.1 \epsilon_{33}$
(011)[111]	$35.6 \epsilon_{33}$	(112)[111]	$41.1 \epsilon_{33}$
(011)[111]	$35.6 \epsilon_{33}$	(112)[111]	$41.1 \epsilon_{33}$
(101)[111]	$35.6 \epsilon_{33}$	(121)[111]	$20.6 \epsilon_{33}$
(101)[111]	$35.6 \epsilon_{33}$	(211)[111]	$20.6 \epsilon_{33}$
(101)[111]	$35.6 \epsilon_{33}$	(211)[111]	$20.6 \epsilon_{33}$
(101)[111]	$35.6 \epsilon_{33}$	(211)[111]	$20.6 \epsilon_{33}$
(110)[111]	0	(211)[111]	$20.6 \epsilon_{33}$
(110)[111]	0	(121)[111]	$20.6 \epsilon_{33}$
(110)[111]	0	(121)[111]	$20.6 \epsilon_{33}$
(110)[111]	0	(211)[111]	$20.6 \epsilon_{33}$

Table 2

Resolved shear stresses on the 24 slip systems corresponding to the family of {123} slip planes; uniaxial strain compression of tantalum along [001].

Slip system {123}	RSS (GPa)	Slip system {123} Cont.	RSS (GPa)
(123)[11̄1]	40.4 ϵ_{33}	(132)[1̄11]	26.9 ϵ_{33}
(123)[111̄]	40.4 ϵ_{33}	(132)[111̄]	26.9 ϵ_{33}
(123)[11̄1̄]	40.4 ϵ_{33}	(132)[11̄1̄]	26.9 ϵ_{33}
(12̄3)[111]	40.4 ϵ_{33}	(132̄)[1̄11]	26.9 ϵ_{33}
(213)[11̄1]	40.4 ϵ_{33}	(231)[1̄11]	13.5 ϵ_{33}
(213)[111̄]	40.4 ϵ_{33}	(231)[111̄]	13.5 ϵ_{33}
(21̄3)[111̄]	40.4 ϵ_{33}	(231̄)[111]	13.5 ϵ_{33}
(213̄)[111]	40.4 ϵ_{33}	(231̄)[1̄11]	13.5 ϵ_{33}
(312)[111̄]	26.9 ϵ_{33}	(321)[1̄11]	13.5 ϵ_{33}
(312̄)[111]	26.9 ϵ_{33}	(321̄)[111]	13.5 ϵ_{33}
(312)[11̄1]	26.9 ϵ_{33}	(321)[11̄1]	13.5 ϵ_{33}
(312̄)[11̄1]	26.9 ϵ_{33}	(321̄)[11̄1]	13.5 ϵ_{33}

(11̄2)[111] 41.1 ϵ_{33} (GPa).
(21̄3)[111] 40.4 ϵ_{33} (GPa).
(01̄1)[111] 35.6 ϵ_{33} (GPa).
(10̄1)[111] 35.6 ϵ_{33} (GPa).

It is clear that the differences are relatively small, and that indeed the (11̄2) slip plane provides the highest resolved shear stress. This explains the easy fluctuation in slip planes that is well known in bcc metals. For instance, the two slip planes (01̄1) and (10̄1) can combine as (11̄2), thus the change from (01̄1) and (10̄1) to (11̄2) increases the stress and should occur easily.

It should also be pointed out that the use of the resolved shear stress criterion has some caveats in bcc metals. The reason for this being the multiple shear stress components that affect the glide of screw dislocations, modifying the dislocation core structure and causing a breakdown of the Schmid law [46–48]. For Ta, a Group VB metal, the screw dislocation core has a sixfold symmetric, non-degenerate structure, with small twinning–antitwinning asymmetry and weak interaction with non-glide applied stress components [49]; therefore, it is reasonable to expect that dislocations will nucleate in available slip systems with a probability associated with the RSS. Sherwood et al. [50] showed that the tension–compression asymmetry produced by core effects is no longer present at 300 K.

3.3. Dislocation activity

MD simulations confirm that the primary mechanism of plastic deformation is the formation of loops, which nucleate at the ledges provided by the void surfaces. A conventional atomistic visualization of the filtered structures reveals that dislocations start to nucleate at a strain of 5.5%, with clear dislocation loop formation at a strain of 5.6%. The evolution of dislocations and void configurations for strains varying from 5.6% to 10% are shown in Fig. 3.

As the applied strain increases, these loops evolve primarily through the high mobility of the edge component. Fig. 4a provides three views along [100], [010], and [001] direction of the same void at an applied strain of 6.5%. It can be seen that at least six loops have formed. They are characterized by straight sides, corresponding to the screw component of the dislocation, and a bowed out front, corresponding to the (primarily) edge component of the dislocation. The shear loop directions are analyzed in Fig. 4b and the directions [1̄1̄], [1̄11], [11̄1], [1̄1̄1] and [1̄11̄] are identified. The other loops are in the back of the void and therefore cannot be seen in this view.

Similar to what was observed by Tang et al. [24], there is some fluctuation in slip planes at the front. Fig. 5 shows details of one loop and the schematic distribution of slip planes.

In spite of {112} slip planes having the highest resolved shear stress (15% higher than {110} planes), nucleated dislocations

evolve mainly on {110} slip planes, since {110} planes are the closest packed planes in the bcc lattice and thus have a relatively lower critical resolved shear stress (CRSS) required for dislocation nucleation. This is also evidenced by the fact that the maximum stacking fault energy of {110} planes is lowest for those planes [23]. {110} slip was also found by Tang et al. for a single void in Ta [24].

While twinning is known to occur in Ta during high strain rate deformation [51], no twinning was found in our simulations. Of course, simulation details might influence twinning. Simulations for a single void have been carried out with much larger samples (tens of millions of atoms) and do not lead to significant differences regarding twinning, but we note that there might be other long-time scale dislocation reactions beyond the reach of atomistic simulations, which might also contribute to twinning. We have also carried out simulations for a single void with a new Ta potential [33] and observed a similar outcome [52]. Of course, there are many factors affecting twinning. Loading orientation will influence twinning [21,52,53], and twinning has been reported for atomistic simulations of voids in Ta under homogeneous [001] tension [23,25], but never for homogeneous [001] compression [21,25]. Use of non-equilibrium shock loading simulations [54] does lead to some twinning for [001] compression resulting from dislocation junctions in a dense dislocation forest. Therefore, appropriate nucleation sites for twinning, such as dislocation junctions and long screw dislocations themselves [20], which are present in experimental conditions but are missing here, might also contribute to the absence of twinning in the current MD simulations. Indeed, addition of grain boundaries as nucleation sites leads to twinning in nanocrystalline Ta [31]. Despite the limitations of atomistic simulations, our results are consistent with recent experimental results [53] for single crystal Ta shock loaded and recovered, showing less than 3% twin fraction for a shock pressure of 55 GPa, which is close to the maximum pressure reached here.

No prismatic loops were observed in the current simulations, in contrast with simulations by Rudd [23] and Tang et al. [24]. They demonstrated that prismatic loops formed in hydrostatic loading when the shear loops expand equally. In the current simulations, the shear loops do not react to form prismatic loops. This reaction needs sufficient space to develop but in our simulations, before the reaction occurs, the shear loops from one void encounter shear loops from voids in the vicinity. Uniaxial compression prevents the intersection of shear loops in the way necessary for prismatic loop formation.

Approximate values for the dislocation velocities were obtained from our MD simulations, by a procedure similar to that described for fcc crystals by Davila et al. [55] and Bringa et al. [20]. The dislocation velocities in uniaxial compressive strain for our tantalum simulation are calculated by tracking the dislocation front as a function of time. Prior to significant dislocation–dislocation interaction, the velocities at a strain rate of 10^9 s^{-1} varied between 600 and 1200 m/s; these values are in the subsonic regime, since for the [001] direction, the transverse sound velocity for Ta is $\sim 2000 \text{ m/s}$ [29]. Dislocation interaction caused a reduction in velocity. Using the same procedure employed by Tang et al. [24], we find that our results are in very good agreement with the linear extrapolation of Deo et al. [56] and Tang et al. [24] for $T = 300 \text{ K}$, as shown in Fig. 6. It must be noted, however, that as Jin et al. [57] and Marian et al. [21] had previously shown, dislocation mobility in bcc metals is extremely complex.

3.4. Total dislocation density using CNA filtering

The total dislocation density, ρ_d , was calculated as the total length of all dislocation lines, l , divided by the volume of our simulated box, V_{def} :

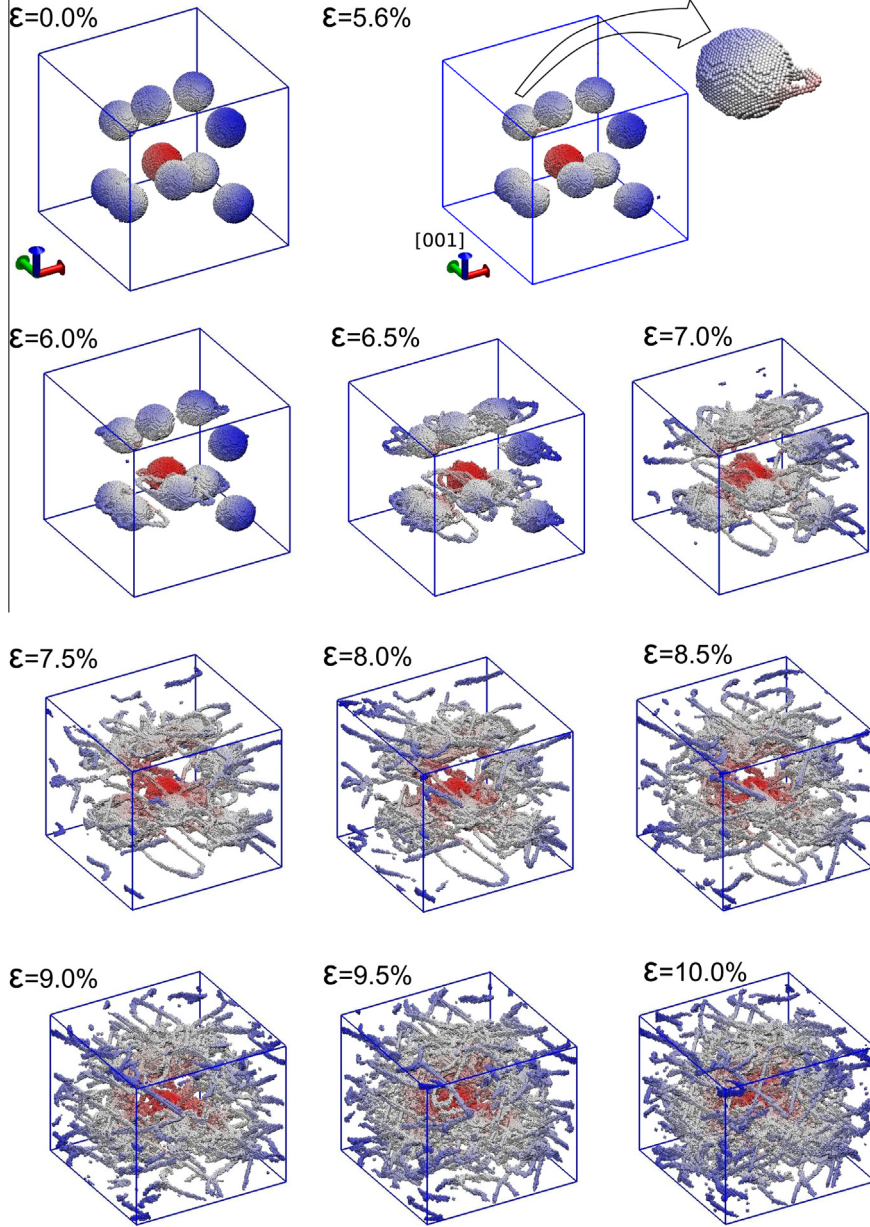


Fig. 3. Evolution of dislocations and voids up to 10% strain. Snapshot at 5.6% includes a zoom with the nucleation of the first dislocation loop. Every 0.5% strain increment corresponds to 5 ps evolution.

$$\rho_d = \frac{l}{V_{def}} \quad (10)$$

The length l can be expressed as:

$$l = \frac{Nd_{nn}}{s} \quad (11)$$

where N is the number of non-bcc atoms associated at a given time-step with dislocation cores, according to the CNA filter, with a cut-off of 0.414 nm [24], and excluding those atoms originally identified as belonging to void surfaces. d_{nn} is the average distance between atoms in the dislocation, here taken to be 0.286 nm, equal to the Burgers vector. s is the cross-section of a typical dislocation, measured by the number of atoms that form the dislocation core for a particular type of filter.

This was done following Bringa et al. [58] and Shehadeh et al. [59], first by computing the number of atoms, N , that belong to dislocation cores, and then substituting Eq. (11) into Eq. (10), yielding:

$$\rho_d = \frac{Nd_{nn}}{sV_{def}} \quad (12)$$

Visualization of non-bcc atoms reveals that the dislocation cores have a typical cross-section of approximately 10 atoms, as seen in Fig. 4. For fcc structures, partial dislocations typically appear with a cross section of 2–4 atoms, when selected with a centro-symmetry filter [59]. The evolution of the dislocation density is shown in Fig. 7. Once plastic activity initiates, the total dislocation density rapidly increases to values consistent with those of metals subjected to high work-hardening (10^{15} – 10^{17} m $^{-2}$), but above 10% strain, the level of noise in our detector makes identification difficult. CNA uses a neighbor search within a spherical shell and, therefore, might provide results which are inappropriate for large uniaxial strains. Consequently, the calculated dislocation densities for strains above 12% should be taken with care. In addition, the CNA filtering gives an increasing contribution of point defects as strain increases, which leads to artificially high dislocation densities.

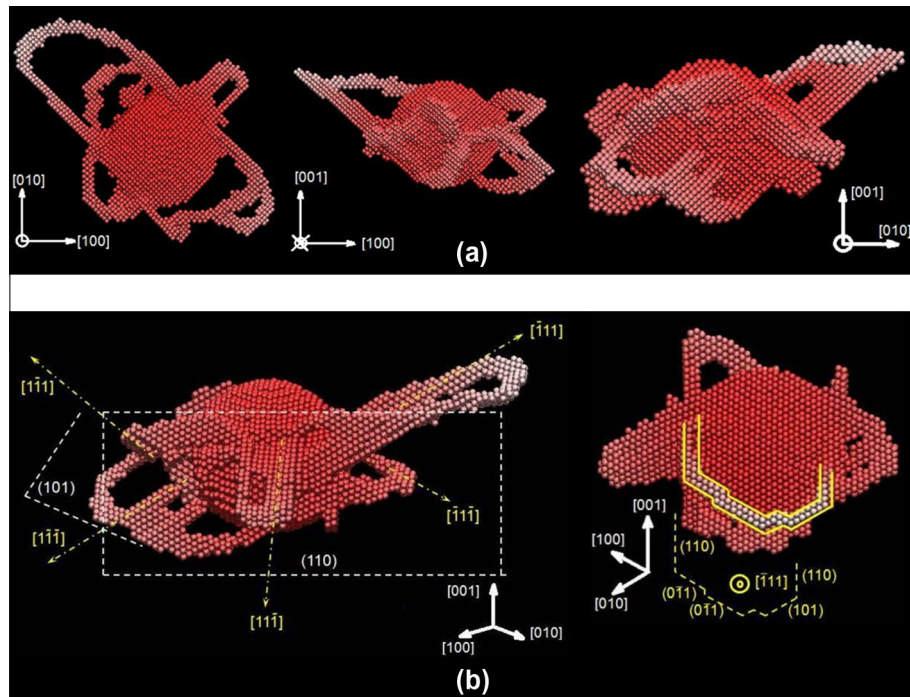


Fig. 4. Snapshot of an isolated void at 6.5% strain. Top sequence shows the void seen from the three principal orientations. Detailed analysis of the dislocation cores reveals the activation of several bcc slip planes and curving of the front.

3.5. Total dislocation density using the dislocation extraction algorithm: DXA

In order to verify the dislocation density estimated from the number of non-bcc atoms, we also measured the density using a recently developed analysis technique. The so-called dislocation extraction algorithm (DXA) [39,40] processes an atomistic simulation snapshot to identify all dislocation defects in the crystal lattice. It outputs a geometric line description of the extracted dislocation network and determines the Burgers vectors of individual dislocation segments. The total dislocation density can be calculated directly from the discretized line representation of the dislocations. In contrast to the counting-based method for estimating the dislocation density described before, the results obtained with DXA are not affected by the presence of non-dislocation defects, which can be effectively eliminated by means of a Burgers circuit test. Fig. 7 shows the measured dislocation density next to the results obtained by CNA only. Both curves are in excellent agreement up to 14% strain. In contrast with the continuously increasing density measured by CNA only, the DXA saturates at high strains. Fig. 8 shows both the conventional atomistic visualization of the simulated system and the defect visualization produced with the DXA tool. In Fig. 9 we produce a set of pictures corresponding to the dislocation forest evolution for strains above 16%. As shown in Fig. 8, the conventional atomistic visualization of the system is essentially saturated with defects above 10% strain, but the DXA tool allows us to see the individual dislocations up to the final strain.

3.6. Mobile dislocation density

In an effort to understand the plastic behavior of our nanoporous sample, the amount of plastic work is an important quantity to be evaluated. Orowan [60] expressed the kinematic relationship between the plastic strain rate $\dot{\gamma}_p$, in terms of the mobile dislocations density, ρ_m , and the mean velocity, \bar{v} , for all dislocation lines in the crystal:

$$\dot{\gamma}_p = b\rho_m \bar{v} \quad (13)$$

where b is the Burgers vector ($b = 0.286$ nm, for bcc Ta).

It is possible to estimate the mobile dislocation density, provided the temperature and stress evolution are known. The temperature evolution is shown in Fig. 10. As plastic activity starts developing, a complex process of emission and motion of dislocation initiates, giving the increase in slope from the purely elastic stage I to stage II, the high slope being the result of the high speed gliding of an important fraction of edge dislocations. The voids are completely collapsed at 14% strain, marking the beginning of stage III, where dislocation movement is more restricted, lowering the slope of the still increasing temperature evolution.

The temperature rise associated with plastic deformation can be expressed in a simplified fashion as:

$$dT = \frac{\beta}{C\rho} \tau_{(t)} d\gamma \quad (14)$$

where C is the specific heat capacity equal to 140 J/(Kg K), ρ is the material density, $\tau_{(t)}$ is the time dependent shear stress, and β is an empirical parameter that represents the fraction of rate of plastic work dissipated as heat [61]. It has been shown that β can take values as low as 0.7 in some cases [62]. The Quinney-Taylor parameter β accounts for the fraction of the work accumulated in the metal (elastic stresses stored through dislocations). Here we assume a value equal to 0.9 based on the recent results by Rittel et al. [63], that show that even though this value is material and condition dependent, for single crystals subjected to high strain rate it takes values very close to unity.

Taking the time derivative and substituting Eq. (13) into Eq. (14), which can be found in detail in Ref. [64], the mobile dislocation density could be expressed as,

$$\rho_m = \frac{C\rho}{\tau_{(t)}\beta b \bar{v}} \frac{dT}{dt} \quad (15)$$

dT/dt is the rate of rise of the temperature, which can be extracted from Fig. 10. b is the Burgers vector, and \bar{v} the average dislocation velocity. This equation can also be derived from a contribution by

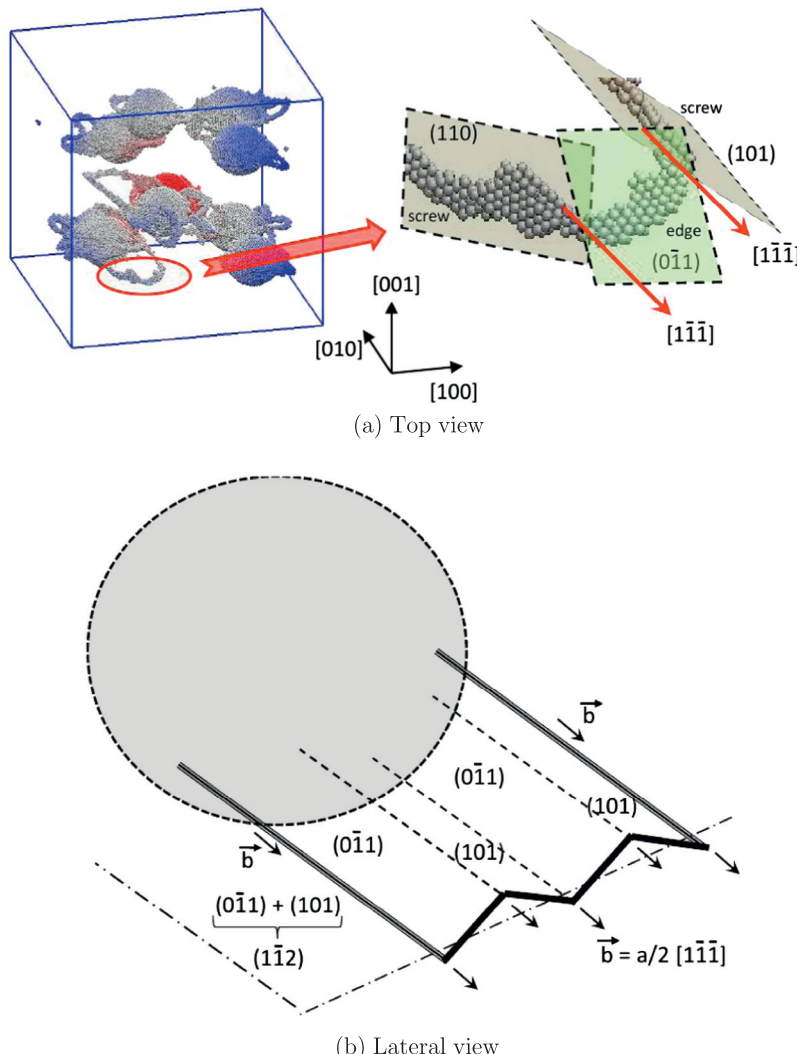


Fig. 5. A detailed representation of the character of dislocations in typical loop is shown in (a) at 6.5% strain. The central part of the loop is an edge dislocation, whereas the sides are screw segments. In (b) the schematic drawing shows how the slip plane $(1\bar{1}\bar{2})$ by virtue of the combination of (101) and $(0\bar{1}1)$ elements, as observed by Tang et al. [24]. The screw components of the dislocation loop can and do cross-slip whereas the front (edge) cannot. This leads, in some cases, to the curving of the front and changing slip planes.

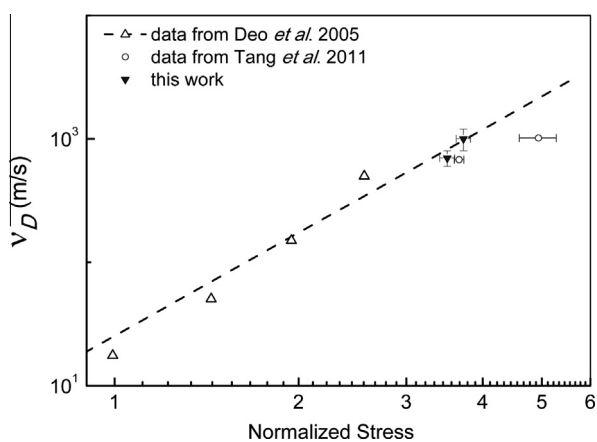


Fig. 6. Dislocation velocity v_D as a function of the stress, normalized with the Peierls Nabarro stress as in [24]: comparison of current results with earlier studies [56,24].

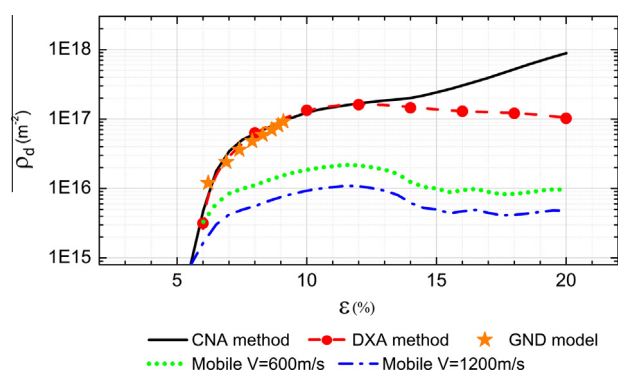


Fig. 7. Dislocation density calculated using different methods as a function of strain. Four computational methods shown: Common Neighbor Analysis (CNA); dislocation extraction algorithm (DXA); geometrically-necessary dislocations (GNDs). There is reasonable agreement among the three procedures (CNA, DXA, and GND). Mobile dislocation densities estimated from plastic heating, assuming two velocities. Mobile dislocations are only a small fraction (~ 0.1) of total dislocation density.

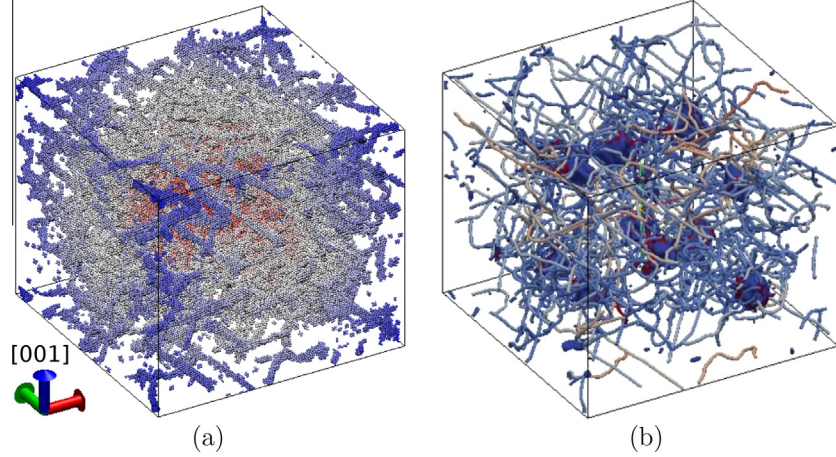


Fig. 8. Snapshot at 12% strain. Comparison of (a) a conventional atomistic visualization using CNA filtering and (b) a geometric line visualization of the dislocations provided by the DXA. In addition to extracting the dislocation line network, the DXA analysis also produces a geometric representation of non-dislocation defects, such as void surfaces.

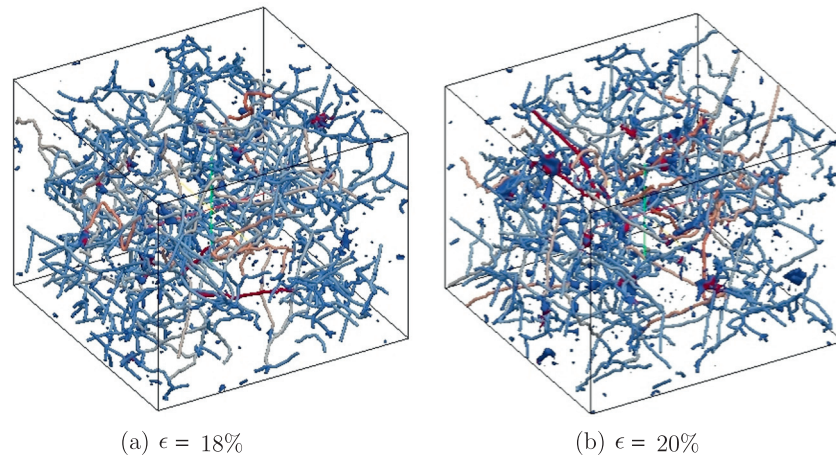


Fig. 9. Snapshots using DXA for 18% and 20% strain. Dislocation density saturates at the full collapse of voids (14%).

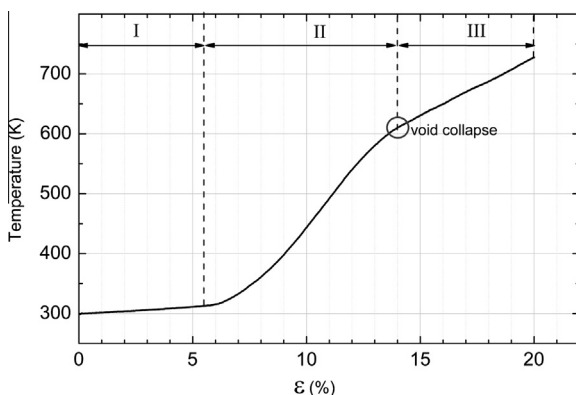


Fig. 10. Temperature evolution showing the three distinctive stages mentioned in the text. Stage I – elastic compression heating, Stage II – plastic heating due to dislocation emission and void collapse, Stage III – plastic heating due to interaction of high density dislocation forest.

Higginbotham et al. [64] for a material with a well defined compliance, and with a single dislocation dipole subjected to rapid shear strain. The results of Higginbotham et al. [64] were for a set of conditions not entirely met in our study, therefore, we emphasize that

the methodology as applied here only provides a rough approximation for the mobile dislocations.

To account for the variable dislocation velocities mentioned before, and considering as a first approximation that screw segments are immobile, the calculation was performed for dislocation velocities with a lower value of 600 m/s and an upper value of 1200 m/s. Fig. 7 shows the mobile dislocation densities obtained for the two dislocation velocities chosen. At this point, it must be emphasized that only the dislocation edge components were used in the current study and, due to their limited mobility, screw components were regarded as immobile and resulting from the advance of the edge components as slip progress.

The length of each shear loop can be roughly estimated by considering that it is composed of three parts, as shown in Fig. 11. The collapse of the voids is enabled by the movement of the edge component of the dislocation loops. In bcc metals, the edge dislocations have a much higher mobility than screw dislocations. The edge dislocation front has a length $L_2 = \pi r / 2\sqrt{2}$, where r is the void radius, being this a first approximation as shown in Fig. 11. The length of the screw components increases from $L_1 = 0$ to $L_1 \sim 10.5$ nm as the loop expands. The fraction of mobile dislocations, f can be approximately expressed as:

$$f = \frac{L_2}{2L_1 + L_2} \quad (16)$$

It decreases from $f=1$ to 0.15 as a first generation of loops leaves the surface and impinges on the opposing voids. As expected from the snapshots of the dislocation evolution, when dislocation activity starts, the total density and the mobile density are similar, but the rapid formation of junctions leads to a decrease in mobile dislocations with respect to the total number of dislocations, with a difference of one order of magnitude at 10% strain.

3.7. Geometrically necessary dislocations

Assuming that the complex interaction of dislocations from different voids can be neglected, the total dislocation length around a collapsing void can be estimated by means of Ashby's concept of geometrically necessary dislocations (GNDs) [65–67]. This can be done in an approximate manner by assuming that the dislocation loops transport matter into the voids [19]. In agreement with Tang et al. [24] and Marian et al. [21,22], loops remain attached to void surfaces during uniaxial compression [68].

Fig. 3 shows that typically, eight dislocation loops are initially nucleated on each void. Subsequently, other loops are also created as the void shrinking proceeds. The length of each dislocation loop

can be roughly estimated by considering that it is composed of three parts, as shown in Fig. 11. Therefore, for every emission i , the total length of the eight loops can be taken as,

$$\Delta L_t^i = 8(2L_1^i + L_2^i) \quad (17)$$

where L_1 is the length of the lateral screw component of each loop and the edge component, L_2 , is considered as defined in the previous section. The configuration is schematically shown in Fig. 11; we assume that each loop expands a distance equal to half the distance between its source and a neighboring void in the vicinity. We also assume, that once these loops reach the loops coming from the neighboring voids, the applied strain is accommodated by a new emission of a loop set. Therefore, the total dislocation length accumulating in the vicinity of the voids is,

$$L_{total}^i = L_{total}^{i-1} + \Delta L_t^i \quad (18)$$

The dislocation contribution for each generation stage (emission and propagation of eight loops) is taken into account by Eq. 17, bearing in mind that the loop front gradually decreases in size as the void radius is decreased. The formation of these eight loops is assumed to shrink the void by a volume ΔV_i for every emission i (Fig. 11)

$$\Delta V^i \approx -2\sqrt{2}\pi(r_{i-1})^2 b \quad (19)$$

then the remaining void volume is

$$V^i = V^{i-1} - \Delta V^i \quad (20)$$

Reestablishing sphericity of voids, the resulting void radius, r_i , after an emission is:

$$r_i = \sqrt[3]{\left(\frac{3}{4\pi}\right)V^i} \quad (21)$$

The strain is computed considering that the decrease in volume due to the shrinking of the ten voids is accommodated by the decrease in the vertical dimension, a_3 , in accordance to the uniaxial strain conditions:

$$V_{sample}^i = V_{sample}^{i-1} - 10\Delta V^i = a_1 a_2 a_3^i \quad (22)$$

where $a_1 = a_2 = 33.03 \text{ nm}$ and a_3 decreases in accordance to the shrinkage of the voids,

$$a_3^i = \frac{V_{sample}^i}{a_1 a_2} \quad (23)$$

The corresponding strain increment $\Delta\epsilon^i$ is:

$$\Delta\epsilon^i = \frac{a_3^{i-1} - a_3^i}{a_3^{i-1}} \quad (24)$$

This calculation is repeated for eight emission generations and the corresponding results are presented in Table 3. The strain increments were subsequently added, so that,

$$\epsilon^i = \Delta\epsilon^i + \epsilon^{i-1} \quad (25)$$

where in the case of $i = 1$, $\epsilon^{i-1} = \epsilon^0 = 0.055$, the strain at the onset of plasticity. Table 3 shows that, after eight generation/emission/propagation steps, the void volume gets reduced to only ten percent of the initial volume.

For simplicity, the work-hardened volume will be considered as the spherical volume limited by the radius R (Fig. 11) and the radius of the void, r_i , therefore it is equal to

$$V_{wh}^i = \frac{4}{3}\pi(R^3 - r_i^3) \quad (26)$$

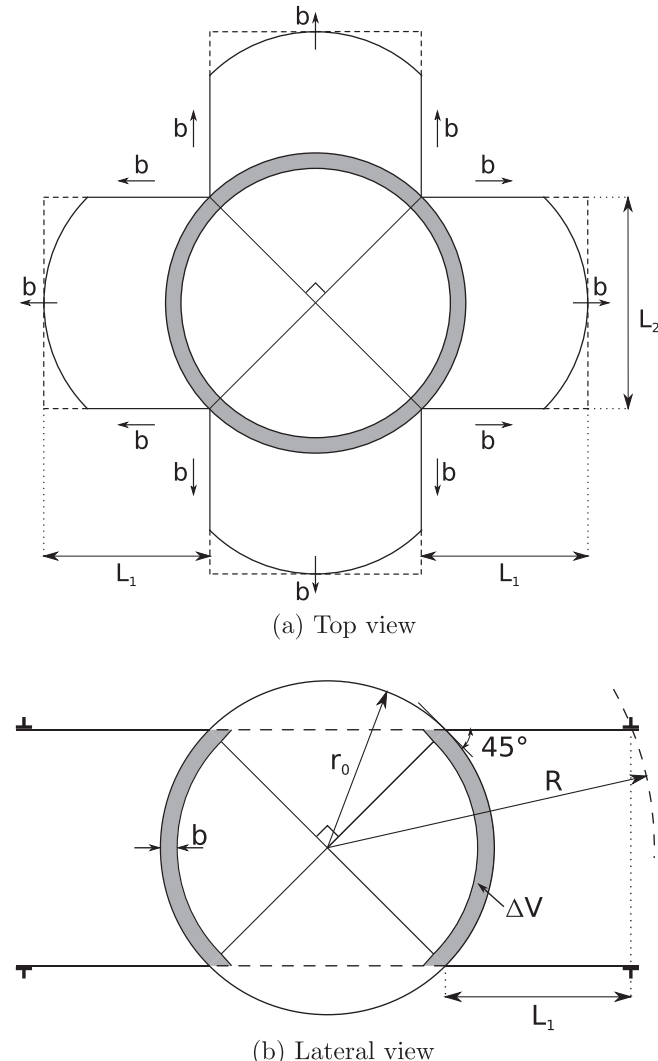


Fig. 11. Top in-plane and lateral schematic representation of the reduction in volume produced by emission of loops, as treated in the geometrically necessary dislocations model.

Table 3

Summary of results for the computation of geometrically-necessary dislocations.

Emission no.	ΔV (nm ³)	V^i (nm ³)	r_i (nm)	V_{wh} (nm ³)	L_{total} (nm)	Strain (%)	ρ_{gnd} (10 ¹⁶ m ⁻²)
0	–	142.5	3.24	–	–	5.5	0
1	–26.7	115.8	3.02	9087	112.8	6.2	1.2
2	–23.2	92.6	2.8	9111	223.2	6.9	2.4
3	–19.9	75.6	2.58	9130	332.1	7.4	3.6
4	–16.9	58.7	2.41	9144	438.9	7.9	4.8
5	–14.8	43.9	2.19	9158	544.4	8.3	5.9
6	–12.2	31.8	1.96	9171	647.7	8.65	7.0
7	–9.8	22	1.74	9180	749.2	8.9	8.1
8	–7.7	14.3	1.5	9188	848.7	9.1	9.2

The dislocation density is finally defined as the ratio of Eqs. (18) and (26).

$$\rho_{GND}^i = \frac{L_{total}^i}{V_{wh}^i} \quad (27)$$

The results of Table 3 are plotted in Fig. 7 for comparison (data points marked with star). It is important to note that this model for GNDs accounts for the successive loop generation needed to accommodate the increasing applied strain. Beyond 10% strain the dislocation forest is too complex to be analyzed with this model.

4. Conclusions

The uniaxial compressive deformation of a porous Ta single crystal with nanometer sized voids (radii ~ 3.3 nm) was modeled by molecular dynamics and analytical methods. This scenario can be achieved by shock loading of nanofoams, re-shocking samples with incipient spall, or re-irradiating samples with high power lasers. The principal results are:

- Plasticity initiates at a lower applied stress and strain than the values reported for a single void [24]. This is in accordance with the stress amplification model of Wu and Markenscoff [43].
- Calculation of the resolved shear stress for all bcc slip systems was performed for a uniaxial strain state and using the stiffness matrix obtained from the potential used [29]. At the onset of plasticity, $\epsilon \sim 5\%$, the shear stress reaches the critical level for the nucleation of dislocation loops. The analysis predicts eight systems with equal shear stress for {110} {111} slip, in agreement with MD results.
- The nanovoid surfaces act as effective sources for dislocations, that nucleate and evolve during the plastic deformation process, rendering strain accommodation by twinning unnecessary. The lack of twinning in our simulations, which reach a maximum pressure of ~ 53 GPa, is consistent with a recent study for a 55 GPa shock of (001) single crystal Ta showing a twinning fraction below few % [53]. Moreover, for a single void, neither [22] nor [24,25] observe twinning for uniaxial compression along the [001] direction, and the void-void interactions do not seem to affect this situation.
- Dislocation velocities were calculated by tracking the advance of their edge component, prior to strong loop-loop interaction. All the calculated velocities are subsonic, and in the range of 600–1200 m/s. Very good agreement was found with the linear extrapolation of the results by Deo et al. [56].
- Dislocation configurations were obtained by the DXA analysis method [40] and compared with an approximate method using CNA.
- Dislocation densities obtained (10^{16} – 10^{17} m⁻²) are comparable to densities in simulations of shock loading in fcc metals at similar strain rates [11,58]. The dislocation densities we find

in our simulations are similar to the predictions of the MTS model, which predicts a saturation dislocation density of $\sim 10^{16}/\text{m}^2$ at a strain rate of 10⁹/s [69]. Moreover, our calculations are also in agreement with experimental results for deformation of Ta at high strain rates [51,70–72], indicating that simulations at relatively short time scales can provide clues to the microstructure of recovered samples for bcc metals.

- The temperature evolution obtained was expressed in terms of the generation and movement of the dislocations and was quantitatively used for estimating the mobile dislocation density which was found to be a fraction of the total density.
- The concept of geometrically necessary dislocations [65–67] was used to estimate the total dislocation length around a collapsing void, leading to a density of geometrically necessary dislocations consistent with dislocation densities estimated by the CNA and DXA estimations.
- Unlike recent porous compaction models [73,74] in which the process of compaction and plasticity are separated and considered to act serially, with compaction occurs first and plasticity later, this study shows that both processes occur in a coupled manner. Therefore, simulations like the ones presented here can be used to help parametrize more advanced compaction models, and current porosity models [75,76] have to be used with care when applied to nanoscale porosity.

Detailed understanding of plasticity in porous metals can lead to the design of materials tailored for specific applications. The work presented here provides an initial study useful for the development of porous compaction model.

Acknowledgements

C.J.R. thanks support from a PFDT scholarship and by UC Laboratories Research Program 12-LR-239079. The help of M. Ribero Vairo in preparation of images and C.-H. Lu on RSS calculations is gratefully acknowledged. E.M.B. thanks support from grant PICT2009-0092 and SeCTyP-UNCuyo. Y.T. and M.A.M. thank the UC Research Laboratories Grant 09-LR-118456. Discussions with X. Markenscoff and V. Lubarda are kindly acknowledged.

References

- [1] J. Biener, A.M. Hodge, A.V. Hamza, L.M. Hsiung, J.H. Satcher, *J. Appl. Phys.* 97 (2) (2005) 024301.
- [2] L. Gibson, M. Ashby, B. Harley, *Cellular Materials in Nature and Medicine*, Cambridge University Press, 2010.
- [3] E.M. Bringa, J.D. Monk, A. Caro, A. Misra, L. Zepeda-Ruiz, M. Duchaineau, F. Abraham, M. Nastasi, S.T. Picraux, Y.Q. Wang, D. Farkas, *Nano Lett.* 12 (7) (2012) 3351–3355.
- [4] E. Fu, M. Caro, L. Zepeda-Ruiz, Y. Wang, K. Baldwin, E. Bringa, M. Nastasi, A. Caro, *Appl. Phys. Lett.* 101 (19) (2012) 191607.
- [5] J.R. Greer, W.C. Oliver, W.D. Nix, *Acta Mater.* 53 (6) (2005) 1821–1830.
- [6] W.D. Nix, J.R. Greer, G. Feng, E.T. Lilleodden, *Thin Solid Films* 515 (6) (2007) 3152–3157.
- [7] J.-Y. Kim, D. Jang, J.R. Greer, *Acta Mater.* 58 (7) (2010) 2355–2363.

- [8] D. Reisman, W. Wolfer, A. Elsholz, M. Furnish, *J. Appl. Phys.* 93 (11) (2003) 8952–8957.
- [9] M. Meyers, L. Murr, K. Staudhammer, *Shock-Wave and High-Strain-Rate Phenomena in Materials*, Marcel Dekker, New York, 1992. p.
- [10] P. Erhart, E. Bringa, M. Kumar, K. Albe, *Phys. Rev. B* 72 (5) (2005) 052104.
- [11] B. Cao, E.M. Bringa, M.A. Meyers, *Mater. Trans. A* 38 (11) (2007) 2681–2688.
- [12] H. Jarmakani, E. Bringa, P. Erhart, B. Remington, Y. Wang, N. Vo, M. Meyers, *Acta Mater.* 56 (19) (2008) 5584–5604.
- [13] J. Cuq-Lelandais, M. Boustie, L. Soulard, L. Berthe, J. Bontaz-Carion, T. de Rességuier, *AIP Conf. Proc.* (2012) 1167–1170.
- [14] J.-P. Cuq-Lelandais, M. Boustie, L. Soulard, L. Berthe, T. De Rességuier, P. Combis, J. Bontaz-Carion, E. Lescouet, Study of spallation by sub-picosecond laser driven shocks in metals, in: *EPJ Web of Conferences*, vol. 10, EDP Sciences, 2010, p. 00014.
- [15] B.C. Tappan, S.A. Steiner, E.P. Luther, *Angewandte Chem. Int. Ed.* 49 (27) (2010) 4544–4565.
- [16] T. Hatano, *Phys. Rev. Lett.* 92 (1) (2004) 015503.
- [17] E. Seppälä, J. Belak, R. Rudd, *Phys. Rev. Lett.* 93 (24) (2004) 245503.
- [18] E. Seppälä, J. Belak, R. Rudd, *Phys. Rev. B* 71 (6) (2005) 064112.
- [19] S. Traiviratana, E.M. Bringa, D.J. Benson, M.A. Meyers, *Acta Mater.* 56 (15) (2008) 3874–3886.
- [20] E.M. Bringa, S. Traiviratana, M.A. Meyers, *Acta Mater.* 58 (13) (2010) 4458–4477.
- [21] J. Marian, W. Cai, V.V. Bulatov, *Nature Mater.* 3 (3) (2004) 158–163.
- [22] J. Marian, J. Knap, M. Ortiz, *Acta Mater.* 53 (10) (2005) 2893–2900.
- [23] R.E. Rudd, *Philos. Mag.* 89 (34–36) (2009) 3133–3161.
- [24] Y. Tang, E.M. Bringa, B.A. Remington, M.A. Meyers, *Acta Mater.* 59 (4) (2011) 1354–1372.
- [25] Y. Tang, E.M. Bringa, M.A. Meyers, *Acta Mater.* 60 (12) (2012) 4856–4865.
- [26] C. Ruestes, E. Bringa, A. Stukowski, J. Rodríguez Nieve, G. Bertolino, Y. Tang, M. Meyers, *Scripta Mater.* 68 (10) (2013) 817–820.
- [27] D. Farkas, A. Caro, E. Bringa, D. Crowson, *Acta Mater.* 61 (9) (2013) 3249–3256.
- [28] S. Plimpton, *J. Comput. Phys.* 117 (1) (1995) 1–19.
- [29] X.D. Dai, Y. Kong, J.H. Li, B.X. Liu, *J. Phys.: Condensed Mat.* 18 (19) (2006) 4527–4542.
- [30] A. Higginbotham, M.J. Suggit, E.M. Bringa, P. Erhart, J.A. Hawreliak, G. Mogni, N. Park, B.A. Remington, J.S. Wark, *Phys. Rev. B* 88 (2013) 104105.
- [31] Y. Tang, E.M. Bringa, M.A. Meyers, *Mater. Sci. Eng.: A* 580 (0) (2013) 414–426.
- [32] R. Zhang, J. Wang, I. Beyerlein, T. Germann, *Phil. Mag. Lett.* 91 (12) (2011) 731–740.
- [33] R. Ravelo, T. Germann, O. Guerrero, Q. An, B. Holian, *Phys. Rev. B* 88 (13) (2013) 134101.
- [34] G. Kimminau, P. Erhart, E.M. Bringa, B. Remington, J.S. Wark, *Phys. Rev. B* 81 (9) (2010) 092102.
- [35] C. Lu, B. Remington, B. Maddox, B. Kad, H. Park, S. Prisbrey, M. Meyers, *Acta Mater.* 60 (19) (2012) 6601–6620.
- [36] H. Jarmakani, B. Maddox, C. Wei, D. Kalantar, M. Meyers, *Acta Mater.* 58 (14) (2010) 4604–4628.
- [37] D. Kalantar, G. Collins, J. Colvin, J. Eggert, J. Hawreliak, H. Lorenzana, M. Meyers, R. Minich, K. Rosolankova, M. Schneider, J. Stöcken, J. Wark, *Int. J. Impact Eng.* 33 (1–12) (2006) 343–352.
- [38] H. Tsuzuki, P.S. Branicio, J.P. Rino, *Comput. Phys. Commun.* 177 (6) (2007) 518–523.
- [39] A. Stukowski, V.V. Bulatov, A. Arsenlis, *Model. Simul. Mater. Sci. Eng.* 20 (8) (2012) 085007.
- [40] A. Stukowski, K. Albe, *Model. Simul. Mater. Sci. Eng.* 18 (8) (2010) 085001.
- [41] W. Humphrey, A. Dalke, K. Schulten, *J. Mol. Graph.* 14 (1) (1996) 33–38.
- [42] A. Henderson, *ParaView Guide, A Parallel Visualization Application*, Kitware Inc., 2007.
- [43] L. Wu, X. Markenscoff, *J. Elasticity* 44 (2) (1996) 131–144.
- [44] B. Cao, D.H. Lassila, C. Huang, Y. Xu, M.A. Meyers, *Mater. Sci. Eng.: A* 527 (3) (2010) 424–434.
- [45] J.F. Nye, *Physical Properties of Crystals: Their Representation by Tensors and Matrices*, first ed., Clarendon Press, Oxford University Press, Oxford [Oxfordshire], New York, 1984.
- [46] V. Vitek, M. Mrovec, R. Gröger, J. Bassani, V. Racherla, L. Yin, *Mater. Sci. Eng.: A* 387 (2004) 138–142.
- [47] R. Gröger, V. Racherla, J. Bassani, V. Vitek, *Acta Mater.* 56 (19) (2008) 5412–5425.
- [48] J. Bassani, V. Racherla, *Prog. Mater. Sci.* 56 (6) (2011) 852–863.
- [49] M. Duebery, V. Vitek, *Acta Mater.* 46 (5) (1998) 1481–1492.
- [50] P. Sherwood, F. Guiu, H.-C. Kim, P.L. Pratt, *Can. J. Phys.* 45 (2) (1967) 1075–1089.
- [51] L. Murr, M. Meyers, C.-S. Niou, Y. Chen, S. Pappu, C. Kennedy, *Acta Mater.* 45 (1) (1997) 157–175.
- [52] D. Tramontina, C. Ruestes, T. Y. E. Bringa, *Comput. Mater. Sci.* (submitted for publication).
- [53] J.N. Florando, N.R. Barton, B.S. El-Dasher, J.M. McNaney, M. Kumar, *J. Appl. Phys.* 113 (8) (2013) 083522.
- [54] D. Tramontina, P. Erhart, T. Germann, J. Hawreliak, A. Higginbotham, N. Park, R. Ravelo, A. Stukowski, M. Suggit, Y. Tang, et al., *High Energy Density Phys.* 10 (2014) 9–15.
- [55] L.P. Davila, P. Erhart, E.M. Bringa, M.A. Meyers, V.A. Lubarda, M.S. Schneider, R. Becker, M. Kumar, *Appl. Phys. Lett.* 86 (16) (2005) 161902.
- [56] C. Deo, D. Srolovitz, W. Cai, V. Bulatov, *J. Mech. Phys. Solids* 53 (6) (2005) 1223–1247.
- [57] Z. Jin, H. Gao, P. Gumbsch, *Phys. Rev. B* 77 (9) (2008) 94303.
- [58] E.M. Bringa, K. Rosolankova, R.E. Rudd, B.A. Remington, J.S. Wark, M. Duchaineau, D.H. Kalantar, J. Hawreliak, J. Belak, *Nature Mater.* 5 (10) (2006) 805–809.
- [59] M.A. Shehadeh, E.M. Bringa, H.M. Zbib, J.M. McNaney, B.A. Remington, *Appl. Phys. Lett.* 89 (17) (2006) 171918.
- [60] E. Orowan, *Proc. Phys. Soc.* 52 (1) (1940) 8–22.
- [61] H. Quinney, G. Taylor, *Proc. Roy. Soc. Lond. Ser. A – Math. Phys. Sci.* 163 (913) (1937) 157–181.
- [62] J. Hodowany, G. Ravichandran, A. Rosakis, P. Rosakis, *Exp. Mech.* 40 (2) (2000) 113–123.
- [63] D. Rittel, A. Kidane, M. Alkhader, A. Venkert, P. Landau, G. Ravichandran, *Acta Mater.* 60 (9) (2012) 3719–3728.
- [64] A. Higginbotham, E.M. Bringa, J. Marian, N. Park, M. Suggit, J.S. Wark, *J. Appl. Phys.* 109 (6) (2011) 063530.
- [65] M.F. Ashby, S.H. Gelles, L.E. Tanner, *Philos. Mag.* 19 (160) (1969) 757–771.
- [66] M.F. Ashby, L. Johnson, *Philos. Mag.* 20 (167) (1969) 1009–1022.
- [67] M.F. Ashby, *Philos. Mag.* 21 (170) (1970) 399–424.
- [68] E. Bringa, V. Lubarda, M. Meyers, *Scripta Mater.* 63 (1) (2010) 148–150.
- [69] N.R. Barton, J.V. Bernier, R. Becker, A. Arsenlis, R. Cavallo, J. Marian, M. Rhee, H.-S. Park, B.A. Remington, R.T. Olson, *J. Appl. Phys.* 109 (7) (2011) 073501.
- [70] L.L. Hsiung, *J. Phys.: Condensed Matter* 22 (38) (2010) 385702.
- [71] W. Wasserbäch, *Mater. Sci. Eng.* 96 (1987) 167–183.
- [72] S. Nemat-Nasser, J.B. Isaacs, M. Liu, *Acta Mater.* 46 (4) (1998) 1307–1325.
- [73] K. Wünnemann, G. Collins, H. Melosh, *Icarus* 180 (2) (2006) 514–527.
- [74] G. Collins, H. Melosh, K. Wünnemann, *Int. J. Impact Eng.* 38 (6) (2011) 434–439.
- [75] A.L. Gurson, Continuum theory of ductile rupture by void nucleation and growth. Part i. Yield criteria and flow rules for porous ductile media, Tech. Rep., Brown Univ., Providence, RI (USA), Div. of Engineering, 1975.
- [76] J. Wen, Y. Huang, K. Hwang, C. Liu, M. Li, *Int. J. Plast.* 21 (2) (2005) 381–395.